Available online at www.sciencedirect.com
SCIENCE DIRECT®
Journal of Computational Physics 194 (2004) 117–139
JOURNAL OF COMPUTATIONAL PHYSICS
www.elsevier.com/locate/jcp

A robust and efficient subgridding algorithm for finite-difference time-domain simulations of Maxwell's equations ☆

A. Vaccari *, R. Pontalti, C. Malacarne, L. Cristoforetti

Centro per la Ricerca Scientifica e Tecnologica, Istituto Trentino di Cultura, Division FCS, Trento I-38050, Italy

Received 1 August 2003; received in revised form 1 September 2003; accepted 3 September 2003

Abstract

Mesh refinement is desirable for an advantageous use of the finite-difference time-domain (FDTD) solution method of Maxwell's equations, because higher spatial resolutions, i.e., increased mesh densities, are introduced only in sub-regions where they are really needed, thus preventing computer resources wasting. However, the introduction of high density meshes in the FDTD method is recognized as a source of troubles as far as stability and accuracy are concerned, a problem which is currently dealt with by recursion, i.e., by nesting meshes with a progressively increasing resolution. Nevertheless, such an approach unavoidably raises again the computational burden. In this paper we propose a non-recursive three-dimensional (3-D) algorithm that works with straight embedding of fine meshes into coarse ones which have larger space steps, in each direction, by a factor of 5 or more, while maintaining a satisfactory stability and accuracy. The algorithm is tested against known analytical solutions.

Keywords: Maxwell's equations; Pulsed FDTD method; Dispersion relation; Group velocity; Nyquist frequency; Low-pass filter

1. Introduction

The finite-difference time-domain (FDTD) solution method of Maxwell's equations is a widely used numerical technique in computational electromagnetics [1], both in the two-dimensional (2-D) and three-dimensional (3-D) cases. Its first formulation goes back to Yee [2]. One writes centered finite difference analogues of the six partial differential equations in the Maxwell's curl equations that, due to the particular choice of the fields' sampling points, are second-order accurate both in space and in time. Examples of these can be found in [1–4]. As an initial value problem (IVP), the FDTD method is subject to a stability condition, the so-called Courant–Friedrichs–Lewy (CFL) condition [3,5]. Also, the

☆ This work was supported in part by the Italian Ministry for Education, University and Research (MIUR 5%).
* Corresponding author. Tel.: +39-0461-314451; fax: +39-0461-810851.
E-mail address: vaccari@itc.it (A. Vaccari).

0021-9991/$ - see front matter
doi:10.1016/j.jcp.2003.09.002

FDTD method needs to be supplemented by a suitable boundary condition (BC) on the outer surface of the computational domain, to overcome finite memory allocation capabilities. To this end various authors developed special BCs [6–13] which, in the FDTD community, are known as absorbing boundary conditions (ABCs) or radiation boundary conditions (RBCs). They permit a mesh truncation with a minimum amount of reflection back into the computational domain. In our work we use second-order Higdon BCs [10,11]. Nowadays, almost invariably, the so-called "pulsed" FDTD method is adopted, that makes use of compact excitation pulses [14,15]. An in-line semidiscrete Fourier transform of the system response is updated at every space sampling point. It is commonly retained that only analyses at frequencies corresponding to wavelengths no shorter than 10 times the space sampling size are meaningful [1,4]. But when, at a given frequency, the structures' electrical density augments, wavelengths are unavoidably shortened. Many efforts then have been made to develop local mesh refinement algorithms for the FDTD method. A brief description of the various approaches can be found in [16]. A reported problem of the various attempts is their tendency to become unstable [16–19]. A common receipt proposed to overcome stability problems is to nest meshes with progressively increasing resolution, say by a factor of 2 each time. Obviously, such an approach further raises the computational burden, a thing we wanted to avoid.

Our effort with the present paper has been to develop a mesh refinement algorithm for the FDTD method which is as economic as possible, both in terms of memory request and in the number of floating point operations. To this end we devised a merging, or coupling, scheme between two FDTD meshes, one of them having an higher resolution by a factor of 5–15 than the other. This results in the algorithm described in Section 2. In the next we will refer to it as the *mesh refinement algorithm* or *subgridding algorithm*. In Section 3 we demonstrate that instability is intrinsic to every mesh refinement and possibly it does not depend on a particular merging scheme. Having recognized the source of instability, in Section 4 we devise a particular technique that permits us to control its onset until the FDTD run has been completed, even though spatially large domains are considered and with satisfactorily accurate results. The technique is based on a spatial-differentiation low-pass filter which is analytically justified. It requires only a certain number of extra floating point operations, but no extra memory allocation. In Section 5 we report experimental numerical results supporting the validity of the algorithm we propose. We point out that it works with straight embedding of high resolution meshes, without resorting to recursive procedures.

2. Mesh refinement algorithm

Starting with a 3-D spatially uniform grid of $N_x \times N_y \times N_z$ cubic Yee cells of edge size δ, we assume a corresponding *time-step* τ, to get a space-time mesh $\mathscr{G}$, such that the CFL stability condition,

$$\tau \leqslant \frac{\delta}{\sqrt{3}c_0}$$

is fulfilled, with c_0 the light speed in vacuo. In particular we always take $\tau = 0.5\delta/c_0$. We refer to $\mathscr{G}$ as the *coarse grid*. In space, its outer surface $\mathscr{S}$ is that of a parallelepiped made of single Yee cell faces.

We now assume that each one of a subset of $n_x \times n_y \times n_z$ contiguous cells in $\mathscr{G}$ – provided that none of their faces lies on $\mathscr{S}$ – is being refined, giving rise to R^3 extra cubic sub-cells with an edge size of δ/R, R a whole number. By introducing a time step of τ/R, we can think at all of the $R^3 \times n_x \times n_y \times n_z$ extra cubic sub-cells as forming a new space-time mesh $\mathscr{G}'$, which we refer to as the *fine grid*.

Note that the same space-time steps ratio holds for both $\mathscr{G}$ and $\mathscr{G}'$, so we do not bother about different CFL conditions. We call R the *mesh refinement factor* and assume it, without loss of generality, to be an odd number too. In this paper we are concerned with values of R from 5 to 15.

In space, the outer surface $\mathscr{S}'$ of $\mathscr{G}'$ is made of single sub-cell faces and it is strictly contained in the volume bounded by $\mathscr{S}$, so we can also say that the fine grid is embedded in the coarse one. We always assume that $\mathscr{S}'$ lies in free space (air), structures being inserted strictly inside $\mathscr{S}'$, on the fine grid, or strictly outside $\mathscr{S}'$, on the coarse one. $\mathscr{S}'$ is the interface across the coarse and fine domains and plays a major role in merging, or coupling, $\mathscr{G}$ and $\mathscr{G}'$. Whatever scheme one chooses to make them interact, the aim is always to get a consistent numerical solution across $\mathscr{S}'$.

By $\vec{E}$, $\vec{H}$ we indicate the electric and magnetic vectors of $\mathscr{G}$ and by $\vec{e}$, $\vec{h}$ those of $\mathscr{G}'$. Single precision floating point variables are allocated for the fields components. Fig. 1 depicts a coarse/fine transition for a part of $\mathscr{S}'$ lying in the yz-plane. The plane views indicated by the letters a, b, c, d, are extracted by displacements of one half a sub-cell edge size along the z-axis. Fig. 1 shows up clearly that there is no reciprocal *space shift* between the coarse and fine grids and, as a consequence, the interface $\mathscr{S}'$ contains sampling points of both $\vec{E}$ and $\vec{e}$ components which are tangential to $\mathscr{S}'$ itself. In what follows we shall indicate such components, collectively, by E^* and e^*. Also, there are some special $\vec{h}$ components, tangential to $\mathscr{S}'$ but shifted $(R+1)/2$ fine space-steps from $\mathscr{S}'$ itself (and R fine space-steps away from each other), which would correspond to similar $\vec{H}$ components if the coarse grid were extended one more cell inside $\mathscr{S}'$. We use such special components, which we henceforth shall collectively indicate by h^*, to update the tangential E^* components on $\mathscr{S}'$. This is the main reason why we choose R to be an odd number. Our FDTD time iterations are composite and each one of them consist – see Fig. 2 for a schematic diagram with $R = 5$ – of a single spatial scanning for the $\vec{E}$, $\vec{H}$ fields (rounded boxes), which we call a coarse sweep, *followed* by R consecutive spatial scannings (numbered from 0 to $R-1$) for the $\vec{e}$, $\vec{h}$ fields (small boxes), which we call fine sweeps. During a sweep, electric and magnetic field component values at every space sampling point are updated, according to second-order accurate finite difference approximations of Maxwell's curl equations. If the algorithm is currently executing the pth fine sweep since it started at $p = 0$, then it has already completed $p \bmod R$ fine sweeps after the last executed coarse one. The latter, on the other hand, is the Pth coarse sweep since the algorithm started at $P = 0$, with $P = (p - p \bmod R)/R$. We assume a reciprocal *time shift* of $\tau(R-1)/2$ between the coarse and fine grids (τ_{shift}), so that on the time axis, we have

$$t_E = P\tau, \quad t_H = t_E + \frac{1}{2}\tau, \quad t_e = p\frac{\tau}{R} - \tau_{\text{shift}}, \quad t_h = t_e + \frac{1}{2}\frac{\tau}{R},$$

the extra shifts between t_E, t_H and t_e, t_h being intrinsic to the FDTD algorithm. Note that we are using different time-steps for the coarse and fine domains, what shortens the overall duration of the FDTD runs. On the other hand some authors [19] use the same time-step, which is that of the fine grid, for stability concerns. Before a coarse sweep – say the Pth in Fig. 2 – is started, we store first the current E^* values in suitable memory locations. After the coarse sweep has been executed, we have new E^* values too, the stored ones now corresponding to the $(P-1)$th. During the R successive fine sweeps – from $p = PR$ onwards in Fig. 2 (remember τ_{shift}) – we use the old and new E^* values as base points in a linear time interpolation, to get the e^* values for each one of the fine sweeps. As can be seen from Fig. 2, for the first $(R+1)/2$ fine sweeps starting at $p = PR$ we have a true interpolation, but for the last $(R-1)/2$ ones we extrapolate outside the time interval spanned by the old and new E^* values. Being the e^* sampling points on $\mathscr{S}'$ spatially denser than those of E^*, as base points for the linear time inter/extrapolation we do not directly use a pair of old and new E^* values. Indeed, from four such pairs lying at the vertices of a square with edge size δ, we fill in, by means of a bilinear space interpolation, a matrix of $R \times R$ base points at every e^* space location inside the square's perimeter. By moving the square at hand and calculating new $R \times R$ base points, we can cover all of the e^* space locations on the six faces of $\mathscr{S}'$. We thus have an "inflowing" information exchange, from $\mathscr{G}$ to $\mathscr{G}'$, marked by upward arrows in Fig. 2. What we are really doing here, is to impose a boundary condition (BC) on $\mathscr{S}'$ for the tangential electric field components in the fine domain. There would not be

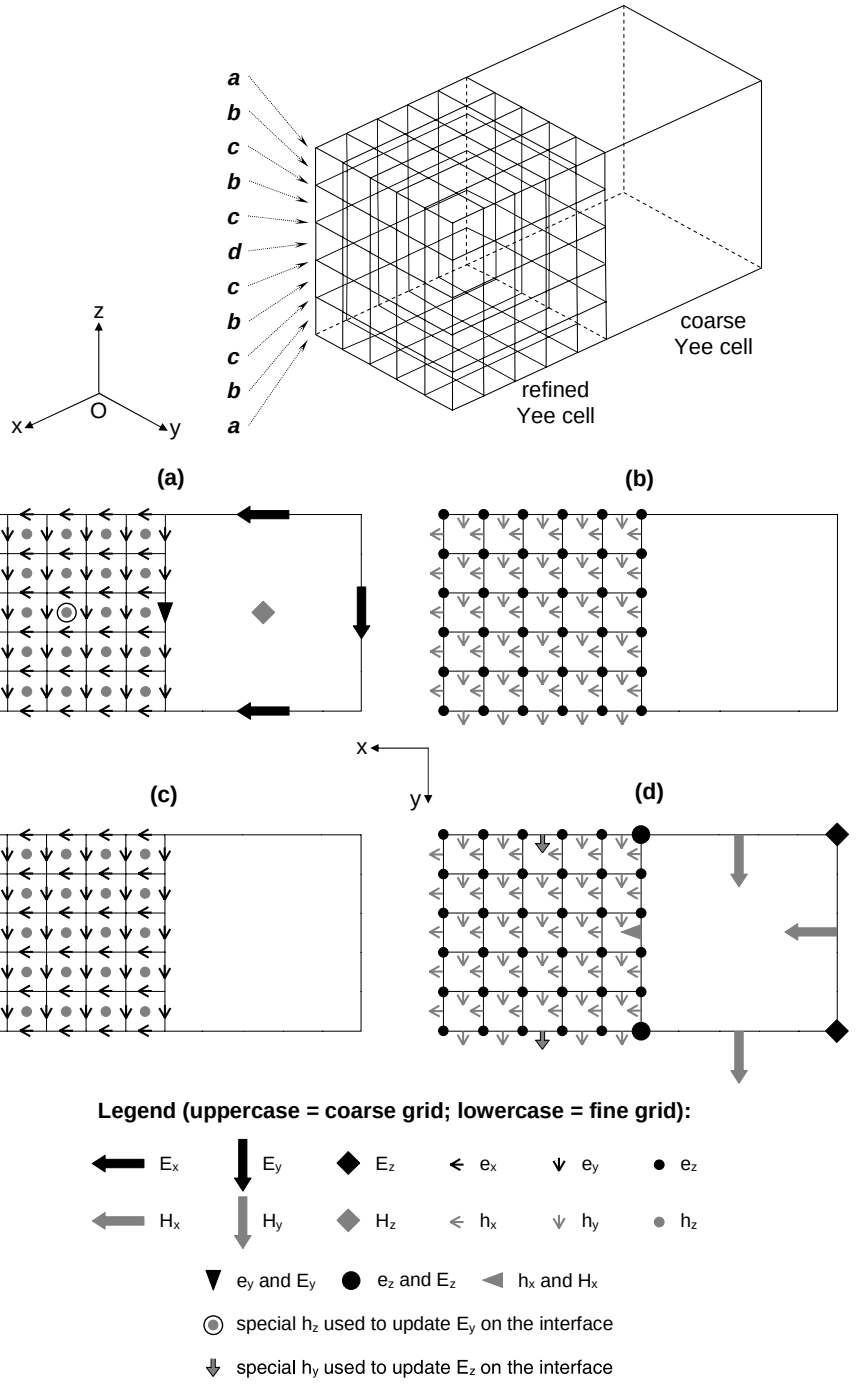

Fig. 1. Fields layout at a coarse/fine grid interface in the yz-plane when $R = 5$.

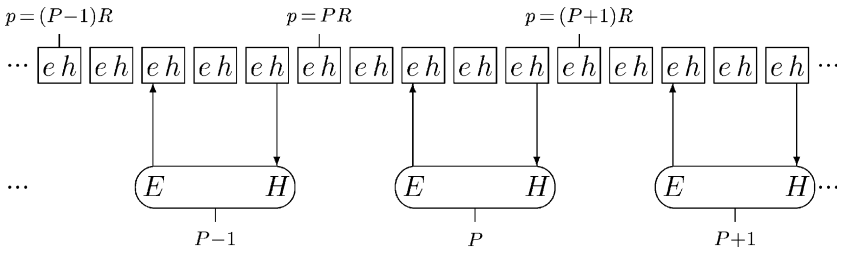

Fig. 2. Timing of the FDTD subgridding algorithm when $R = 5$.

any other mean to get those values via the difference equations of the Yee algorithm. An "outflowing" information exchange, from $\mathscr{G}'$ to $\mathscr{G}$, marked by downward arrows in Fig. 2, occurs when the h^* subset of values, calculated in the course of every Rth fine sweep (the last one of each series), is employed to update the E^* values when a coarse sweep is started. To this end, the last fine sweep h^* values are first passed on suitable $\vec{H}$ memory locations in $\mathscr{G}$ and then directly used in the successive coarse sweep.

To summarize, our basic FDTD subgridding algorithm – with a bidirectional coupling scheme between $\mathscr{G}$ and $\mathscr{G}'$ – is made of the following sequence of computing steps:

(a) Store the current h^* values in suitable memory locations. This requires about $4 \times (n_x n_y + n_y n_z + n_x n_z) \times F$ bytes of memory, where F is the size of a single field component variable. For us, $F = 4$ bytes.
(b) Store the current E^* values in suitable memory locations. This requires about the same amount of memory as step (a).
(c) Update the $\vec{E}$ values in $\mathscr{G}$ by using the appropriate set of finite difference equations. Notice that to get the new E^*s, use is made of the values stored in step (a). Add excitation signals, if any.
(d) Apply the chosen absorbing boundary conditions to the tangential $\vec{E}$ values on $\mathscr{S}$ to model an infinite medium.
(e) Update the $\vec{E}$ Fourier transforms in $\mathscr{G}$.
(f) Update the $\vec{H}$ values in $\mathscr{G}$, including those normal to $\mathscr{S}'$, by using the appropriate set of finite difference equations. Add excitation signals, if any.
(g) Update the $\vec{e}$ values in $\mathscr{G}'$ by using the appropriate set of difference equations, but excluding the e^* values on $\mathscr{S}'$. Add excitation signals, if any.
(h) Calculate updated e^* values by bilinear space interpolation and linear time inter/extra-polation. Note that, to this end, the values stored in step (b) and calculated in step (c) are used.
(i) Update the $\vec{e}$ Fourier transforms in $\mathscr{G}'$.
(j) Update the $\vec{h}$ values in $\mathscr{G}'$ by using the appropriate set of finite difference equations. If this is the last fine sweep, part of the values obtained here, and precisely the h^* ones, will be copied in suitable memory locations as prescribed by step (a).
(k) Repeat steps from (g) to (j) again for a total of R times.
(l) Repeat steps from (a) to (k).

The sequence from (a) to (k) represents an FDTD time iteration, those from (c) to (f) and from (g) to (j) are a coarse and a fine sweep respectively. The overall number of FDTD iterations needed by a program run depends on the spatial extensions of $\mathscr{G}$ and $\mathscr{G}'$, and on the particular structures that are modelled on them. Because we are using the pulsed FDTD method, we must wait until the excitation signal response pulses have decayed at every sampling point and truncation of the semidiscrete Fourier transforms is now permitted. All this, *provided that the above algorithm has been rendered stable*, a matter we deal with in Section 4. As to the excitation signals, we use compact pulses on a time interval $(0, T)$ of the type [14,15]:

$$S_1(t) = \begin{cases} 0, & t < 0, \\ H\left[1 - \cos\left(\frac{2\pi t}{T}\right)\right]^3, & 0 < t < T, \\ 0, & t > T, \end{cases}$$

which is a *non-zero* mean value smooth pulse, continuous in $t = 0$ and $t = T$ with its first five derivatives, or of the type

$$S_2(t) = \begin{cases} 0, & t < 0, \\ K\left[1 - \cos\left(\frac{2\pi t}{T}\right)\right]^2 \sin\left(\frac{2\pi t}{T}\right), & 0 < t < T, \\ 0, & t > T, \end{cases}$$

which is a *zero* mean value smooth pulse, continuous in $t = 0$ and $t = T$ with its first four derivatives. Both H and K are normalization constants which here we choose such that the amplitude spectra of $S_1(t)$ and $S_2(t)$ are 1 at their maximum. Moreover, T is set to $1/f_a$ with $S_1(t)$ and to $2/f_a$ with $S_2(t)$, in such a way the significant part of their amplitude spectra will embrace the value f_a, the frequency of analysis. Choosing to double T with $S_2(t)$ is a small correction to compensate for the fact its amplitude spectrum vanishes when $f \to 0$. To overcome problems with static fields of the type discussed in [15], in the next we will use $S_2(t)$.

3. Stability analysis of the mesh refinement algorithm

When grids with different space-time resolutions are interacting, fulfilling the CFL condition inside each single grid is not enough for the overall stability of the FDTD algorithm. The CFL condition addresses the initial value problem (IVP) only, i.e., for the wave propagation as if it took place in an unbounded spatial domain. Special stability analysis is required when BCs are additionally imposed on the solution and one is then faced with an initial boundary value problem (IBVP). In the FDTD method the BCs typically concern with the modelization of an unbounded spatial domain and one speaks of ABCs or RBCs. A large literature exists that analyzes the well-posedness and stability of a hyperbolic IBVP from an analytical and numerical point of view, respectively [10,11,20–23]. All the various BCs proposed for the spatial truncation of the FDTD computational domain must obey, more or less implicitly, to further stability criteria than the simple CFL condition.

Undoubtedly, when grids with different space-time resolutions are coupled together one has to deal, from a numerical point of view, with extra BCs at the grids' interface. In fact, field components values are repeatedly exchanged across them, but with each grid having its own dispersion properties. For a Yee FDTD mesh having cubic cells of edge size δ and time step τ, the following dispersion relation holds in an homogeneous medium:

$$\sin^2\left(\frac{\eta}{2}\right) = \left(\frac{c_0\tau}{\delta}\right)^2 \left\{ \sin^2\left(\frac{\xi_x}{2}\right) + \sin^2\left(\frac{\xi_y}{2}\right) + \sin^2\left(\frac{\xi_z}{2}\right) \right\}. \tag{1}$$

Phase velocity in the continuous limit is c_0, $\eta = \tau\omega$ with ω the angular frequency, $\xi_i = \delta k_i$ $(i = x, y, z)$ with $k = (k_x^2 + k_y^2 + k_z^2)^{1/2}$ the wave number. Graphs of (1) are depicted in Fig. 3 for the 1-D case: $\xi_y = \xi_z = 0$. The lower curve refers to the original grid (the coarse one), the upper curve refers to a refined grid with $R = 5$, i.e. with a space step of δ/R and a time step of τ/R. For both, the same ratio $c_0\tau/\delta = 0.5$, satisfying the CFL condition, has been chosen. In drawing the graphs, for the sake of clarity, only those parts of (1) relevant for the discussion are plotted. Moreover, it is enough, due to the space-time discreteness, to consider values of ξ, η in a range with endpoints given by the Nyquist limits of the sampling. That range would be $[-\pi, \pi]$ for a single grid alone, but becomes $[-R\pi, R\pi]$ when grids with different resolutions are compared. The dispersion relation of the coarse grid has, therefore, to be analytically extended beyond its natural upper bound at $\xi = \pi$ by taking into account the "aliasing". The result is that negative slope parts

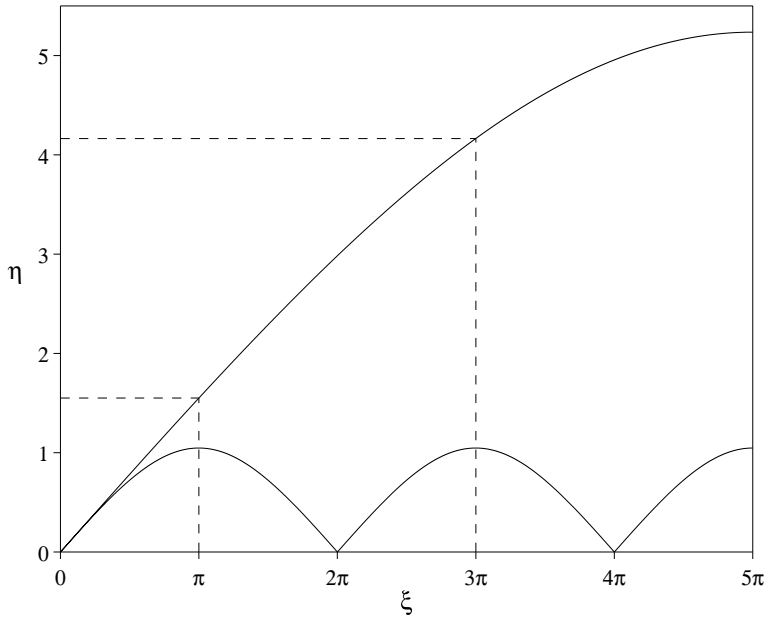

Fig. 3. Dispersion curves of coarse and refined grids when $R = 5$.

appear now, corresponding to positive slopes on the refined grid. We claim that is the basis of subgridding instability, because positive slope means forward waves, while negative slope means backward waves, i.e., the two grids have conflicting behaviors. For a plane electromagnetic wave coming from a left region 1 and entering a right region 2, the normal incidence reflection coefficient $\rho_{1,2}$ at the interface is given by

$$\rho_{1,2} = \frac{1 - \alpha_{2,1}}{1 + \alpha_{2,1}},$$

where $\alpha_{2,1}$ is the ratio of the phase velocities in regions 2 and 1, respectively. If the two media are dispersive and medium 1 behaves like the refined grid and medium 2 like the coarse one, it would be more appropriate to consider wave packets and *group velocity*. Generalizing what can be seen from Fig. 3, ξ values which correspond to the maxima of the coarse grid dispersion curve and are the starting points of negative slopes too (such as π or 3π), give rise to the following set of frequency values:

$$f_{R,q} = \frac{R}{\pi\tau} \arcsin\left[\frac{1}{2}\sin\left(\frac{q\pi}{2R}\right)\right] \tag{2}$$

read on the refined grid dispersion curve. Here, $R = 5, 7, 9, \ldots$ and q takes on odd values from 1 to $R - 2$. At these *critical* frequencies $\rho_{1,2} = 1$ and *total reflection* occurs. This happens because the group velocity of medium 2 vanishes there, but not that of medium 1 and $\alpha_{2,1} = 0$. Even worse, there are points beyond the values given by (2) – as in the negative slope intervals $(\pi, 2\pi)$ and $(3\pi, 4\pi)$ of the ξ axis in Fig. 3 – at which $\rho_{1,2}$ becomes infinity for wave packets, because $\alpha_{2,1} \to -1$. On the other hand if signals of interest had a maximum frequency content well below the smallest of (2), i.e., well below $f_{5,1}$ (remember we start with $R = 5$), spurious reflections at the grids' interface would almost be zero and instability could be avoided. This is not the case in any practical situation, especially in the pulsed FDTD method, and even the smallest contributions at the higher frequencies can give rise to instabilities. The following table lists numerical values in GHz of the critical frequencies obtained from (2) when $R = 5, 9$ and 13 and $\tau = 16.667$ ps.

$R \setminus q$	1	3	5	7	9	11
5	14.8	39.8	–	–	–	–
9	14.9	43.4	67.6	84.1	–	–
13	15.0	44.3	71.5	95.2	113.9	125.9

We now proceed to a formal analysis of the numerical stability of the subgridding algorithm in the 1-D case. To this end, use is made of the so-called *normal modes*, "eigenmodes" or, simply, Fourier modes [10,11,20–23]. These are solutions of the form:

$$w_{\ell,p} = \kappa^{\ell} v^{p},$$

where ℓ and p are spatial and temporal discrete indices ($p \geqslant 0$), while κ and v are complex numbers. Part of the BCs employed in the subgridding algorithm consists in the time inter/extra-polation of the refined electric field values at the grids interface. By indicating with lower/upper case letters fine/coarse quantities, the corresponding numerical equation is

$$\kappa^{\ell} v^{p} = K^{L} N^{(p-p \bmod R)/R} \left\{ 1 + \frac{N-1}{R} (p \bmod R) \right\},$$

where, as usual, R is the mesh refinement factor. The second term in the curly brackets represents the time derivative used for the first order approximation, while the temporal index of the coarse grid has been expressed by using that of the refined one. If we consider purely oscillatory [1] modes:

$$\begin{aligned} v &= \mathrm{e}^{-\mathrm{i}\omega\tau/R} \quad \text{and} \quad N = \mathrm{e}^{-\mathrm{i}\omega\tau} \;\Rightarrow\; N = v^{R}, \\ \kappa &= \mathrm{e}^{+\mathrm{i}k\delta/R} \quad \text{and} \quad K = \mathrm{e}^{+\mathrm{i}k\delta} \;\Rightarrow\; K = \kappa^{R}, \end{aligned}$$

and assume that, at the grids interface, $\ell = L = 0$, we obtain the following set of R equations, representing the BC as a consequence of grids coupling:

$$v^{-m} \left\{ 1 + m \frac{v^{R} - 1}{R} \right\} = 1, \quad m = 0, 1, \ldots, R-1, \tag{3}$$

where m stands for $p \bmod R$. Now, a fundamental result concerning the stability of numerical hyperbolic IBVPs [11,21] prescribes that, for each v, modes entering the domain cannot fulfill the BCs which, in our case, are given by (3). But (3) itself does not depend on κ and, whichever v can be ($v \neq 0$), it always has a solution when $m = 0$, even for κ representing an "incoming" [2] mode. What demonstrates the intrinsic instability of the subgridding algorithm. The previous discussion suggests that if we were able to impose a filtering action at the grids coupling level, such as to confine signals bandwidth well below $f_{5,1}$ of (2), the unstable behavior of the subgridding algorithm could be mitigated. The goal is to extend the number of FDTD time iterations as long as is possible, while retaining a satisfactory accuracy in the results, by forcing both grids to work in the linear regions of their dispersion curves. The subject of the following section is the

[1] The stability criterion for IBVPs is by no means limited to κ, v values on the unit circle in the complex plane. In fact, $|v| \geqslant 1$ ($|v| > 1$ implies an exponential growth with time). However, if one fails to meet the criterion for such purely oscillatory modes, instability arises.

[2] For an oscillatory mode to be "incoming", the relative signs of ω and k from the dispersion curve, in the imaginary exponents, are involved.

way we employ to filter signals. However, we only apply it to the h^* field components (see Section 2), what contributes to keep low the computational burden.

4. Low-pass filtering by spatial differentiation

As stated in the previous section, we have the need to low-pass filter the h^* field components involved in our grid coupling scheme. To avoid any phase shift is a fundamental issue here, but acting in the time domain would impose us an off-line data processing, a task obviously impossible during an FDTD run. In fact, the complete knowledge of the signal is required if a recursive numerical filter without time delay has to be implemented. On the contrary, by relaxing some of the constrains on the filter response such as passband flatness, roll-off rate and maximum allowable attenuation, we devised an in-line spatial-differentiation-based filtering technique – formula (5) below – which, we will demonstrate, largely improves stability. It will be applied to every h^* component *before* the storage of step (a) in Section 2.

We start with the following representation of a generic scalar solution $\mathscr{U}$ of the wave equation, as described in [24]:

$$\mathscr{U}(r,\theta,\phi,t) = \sum_{n=0}^{\infty} \frac{u_n(\theta,\phi,t')}{r^{n+1}}, \quad \text{with } t' = t - \frac{r}{c_0}, \tag{4}$$

where r, θ, ϕ are the spherical coordinates of a point in space and the u_n are real valued functions which all depend on the shape of u_0, the so-called "radiation field" of the pulse $\mathscr{U}$ [24]. Here, $\mathscr{U}$ stands for h_x^* or h_y^* or h_z^*.

Expansion (4) holds if all the sources of the electromagnetic field, acting from some definite instant of time onwards, are confined in a bounded region around the origin $r = 0$.

Being interested here in the frequency content of $\mathscr{U}$, we analyze the spectrum of each of the numerators in the terms of (4):

$$w_n(\theta,\phi,\omega) = \int_{-\infty}^{+\infty} \mathrm{e}^{-\mathrm{i}\omega t'} u_n(\theta,\phi,t')\,\mathrm{d}t', \quad n = 0,1,2,\ldots,$$

where i is the imaginary unit and the angular frequency ω is the dual variable of t'. By further expanding each of the $w_n(\theta,\phi,\omega)$ in a series of spherical harmonics:

$$w_n(\theta,\phi,\omega) = \sum_{\ell=0}^{\infty} \sum_{m=-\ell}^{+\ell} a_{n,\ell,m}(\omega) Y_{\ell,m}(\theta,\phi),$$

with real coefficients $a_{n,\ell,m}$ that will depend only on ω, it shows up that we can think at $\mathscr{U}$ as being composed of a denumerable set of "plane waves" emanating from the origin:

$$a_{n,\ell,m}(\omega)\,\mathrm{e}^{\mathrm{i}(\omega t - kr)},$$

$k = \omega/c_0$ being their wave number. Each of these waves is weighted by a factor depending on $1/r^{n+1}$ and on the direction defining angles θ and ϕ.

Now suppose we want to artificially modify the amplitudes $a_{n,\ell,m}$ of the plane waves by using an ad hoc multiplying function $\mathscr{F}(\omega)$ that suppresses high frequencies. In other words we want to pass to new amplitudes $\mathscr{F}(\omega)a_{n,\ell,m}(\omega)$ for any given n, ℓ, m. Returning back to the $u_n(\theta,\phi,t')$ by taking into account the filtering function, we get

$$u_n^{\mathscr{F}}(\theta,\phi,t') = \frac{1}{2\pi} \int_{-\infty}^{+\infty} \mathrm{e}^{\mathrm{i}\omega t'} \mathscr{F}(\omega) w_n(\theta,\phi,\omega)\,\mathrm{d}\omega.$$

If $\mathscr{F}(\omega)$ is taken to be a non-negative real valued even function of ω, we introduce no phase shift at all, while preserving the real value character of the u_n themselves. By expanding $\mathscr{F}(\omega)$ in a Taylor series at $\omega = 0$ and by making use of the well-known properties of Fourier transforms, we get

$$u_n^{\mathscr{F}}(\theta, \phi, t') = \sum_{k=0}^{\infty} (-1)^k \mathscr{F}_{2k} \frac{\partial^{2k} u_n(\theta, \phi, t')}{\partial t'^{2k}},$$

where the $\mathscr{F}_{2k}$ are the Taylor coefficients of $\mathscr{F}$ (with $\mathscr{F}_0 = 1$). If the t' derivatives are made keeping r fixed, the same result will hold for the solution $\mathscr{U}(r, \theta, \phi, t)$ of the wave equation in (4), being now possible to exchange the derivatives with the $1/r^{n+1}$ factors and with the summation operators. Moreover, by the wave equation itself, second-order time derivatives can now be replaced with the Laplacian operator $c_0^2 \vec{\nabla}^2$ (followed by a c_0^2 multiplication) as well.

As the final result, we can write approximations of the low-pass filtered field component $\mathscr{U}_{\mathscr{F}}(r, \theta, \phi, t)$, by using the unfiltered values $\mathscr{U}(r, \theta, \phi, t)$ of the same field component furnished at any given time step by the FDTD algorithm itself

$$\mathscr{U}_{\mathscr{F}}(x, y, z, t) = \mathscr{U}(x, y, z, t) + \sum_{n=1}^{\infty} (-1)^n \mathscr{F}_{2n} (c_0^2 \vec{\nabla}^2)^n \mathscr{U}(x, y, z, t), \tag{5}$$

where $(c_0^2 \vec{\nabla}^2)^n$ indicates a repeated n-fold application of the Laplacian operator, which now can be expressed in cartesian coordinates, what is more appropriate for the FDTD formulation. Time derivatives are intentionally avoided in (5), because they would have required values ahead in time, that have not been calculated yet at the current FDTD time step. The spatial partial derivatives involved in (5) are all of even order, the maximum order depending on the number of terms retained in the summation. All the partial derivatives can be numerically implemented by second-order accurate centered difference expressions. Due to their stencil, a mesh refinement factor of $R = 5$ permits to retain terms up to $\mathscr{F}_4$ included only: higher-order terms, if desired, require higher mesh refinement factors. In fact, one should keep in mind that, in order to numerically implement a mixed partial derivative of order $2p$, $2q$, $2r$ with respect to the x, y, z variables, values are required that are p, q, r space steps apart from the central location along the corresponding coordinate axes, in both the positive and negative direction. As a rule R must be such that $R \geqslant 2n + 1$ for $n = 0, 1, 2, \ldots$. The filter order is expressed by $2n$ ($n = 0, 1, 2, \ldots$). Eq. (5) is our basic tool to give a good stability behavior to the mesh refinement algorithm described in Section 2.

As far as the filtering function $\mathscr{F}(\omega)$ is concerned, we opted for a normalized to unity first kind Chebychev polynomials expansion of an ideal low-pass filter response – which is 1 for $|\omega| < \omega_c$ and 0 for $|\omega| > \omega_c$, where $\omega_c \equiv 2\pi f_c$ is the cut-off (angular) frequency – and equated the coefficients of the various powers of ω with the coefficients $\mathscr{F}_{2n}$ in (5). The interval of the polynomial expansion is taken on the span $[-\omega_s, \omega_s]$, where

$$\omega_s \equiv 2\pi f_s = \frac{\pi R}{\tau}$$

is the Nyquist angular frequency limit of the refined grid and τ – as usual – the time step of the coarse one. However, due to the slow convergence rate of a polynomial expansion, f_c and the "true" frequency half-span f_s' may be empirically chosen to fit the resulting filter response curve to a more convenient shape for the purpose at hand. In the following section we will employ ideal filter response approximations by Chebychev polynomials *up to* the second – i.e., up to $n = 1$ in (5) –, fourth (up to $n = 2$) and eighth degree (up to $n = 4$) as given by the curves shown in Fig. 4. For the second degree (parabolic filter) we choose always the intercept f_{null} of the parabola at a frequency value of 0.25 f_s. For both the other we choose always $f_c = 8$ GHz (the vertical dashed line in the figure) and a true half-span $f_s' = 0.4 f_s$. The shape of the

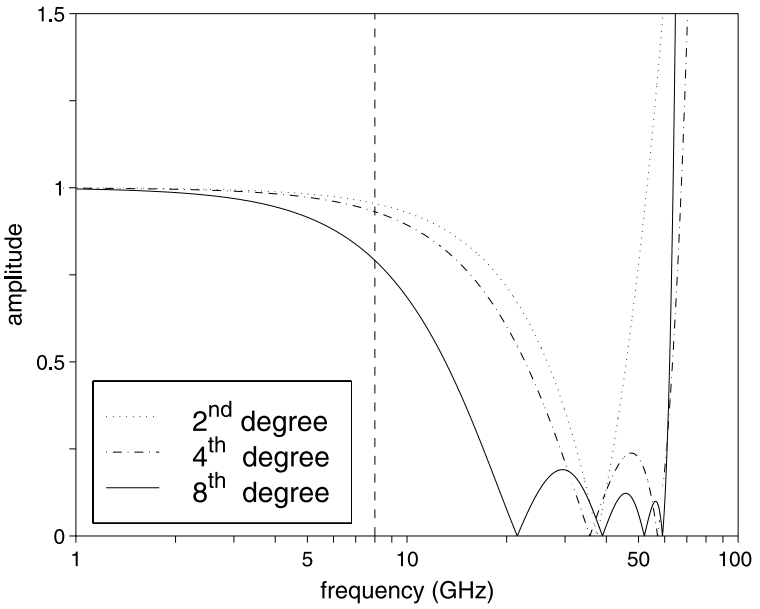

Fig. 4. Ideal low-pass filter response curve approximations when $R = 5$.

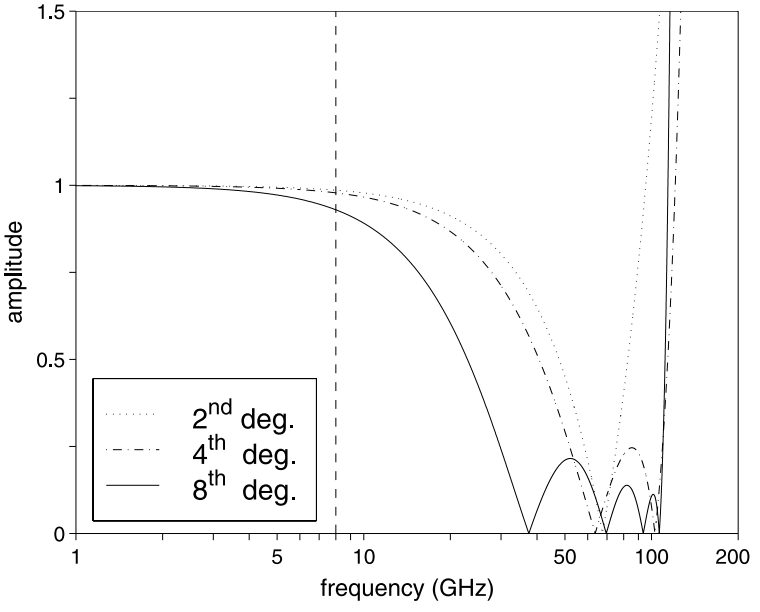

Fig. 5. Ideal low-pass filter response curve approximations when $R = 9$.

curves depends on τ and R. Those in Fig. 4 refer to a coarse grid with $\tau = 16.667$ ps and a refinement $R = 5$ (i.e., $f_{\text{null}} = 37.5$ GHz, $f_s' = 60$ GHz). Also, note that absolute values are reported. In Fig. 5 it is shown how the shapes change when $R = 9$ keeping τ fixed (now $f_{\text{null}} = 67.5$ GHz, $f_s' = 108$ GHz). Negative values of the response curve imply a phase shift of 180°. We do not bother about this and rely indeed on the fact that the

amplitude attenuation effect will prevail, within certain limits. Also notice that, beyond f'_s, the higher the polynomial degree in the Chebychev expansion, the steepest the growth of the response curve. Strictly speaking, a filter of order greater than 4 requires smoother signals than $S_1(t)$ and $S_2(t)$ of Section 2 and the greater the filter order, the smoother the signals required, with an obvious relation between the continuity class of the pulses and the maximum order of the spatial derivatives involved by the filter. Increasing the smoothness would imply rising further the exponents outside the square brackets in the definitions of $S_1(t)$ and $S_2(t)$ in Section 2, with a corresponding increase in the frequency extension of their spectra. However, in the Section that follows we continue to use an excitation signal like $S_2(t)$ – continuous with its first four derivatives – even though the employed filter order is 8. We rely on the fact that, being the method discrete, singularities are smeared out and any superposed high frequency noise due to this choice will not significantly affect the results we get.

It should be pointed out, to conclude this section, that our analysis leading to (5) strictly holds if, in the problem at hand, all the sources of the electromagnetic field are completely contained in the fine grid. This is indeed the case when dealing with accurate modeling of complex sources (e.g., antennas). However, in other practical applications the above condition may not be satisfied, e.g., when subgridding is used to embed high permittivity scatterers. If *part* of the sources lie outside $\mathscr{S}'$, it is still possible to apply (5) with satisfactory results concerning stability and accuracy. This will be demonstrated in the following section for the scattering from a dielectric sphere in a plane incident wave field, the sources of which are, obviously, at infinity. We made numerical tests for such a problem in a geometry that strongly stressed the coupling mechanism between $\mathscr{G}$ and $\mathscr{G}'$ obtaining, by use of (5), good results.

5. Numerical experiments with the mesh refinement algorithm

To assess the stability and accuracy of the proposed subgridding algorithm, we performed two groups of tests. The first group concerns with the comparison, in the case of a plane TEM wave falling, along the z-axis, on a sphere of radius 4.5 cm and $\varepsilon_r = 4$ (relative electric permittivity), between the numerical FDTD solution and the analytical one at a frequency of 2.5 GHz. We obtain the analytical solution for this electromagnetic problem by implementing the frequency-domain, summed-mode series technique of Stratton [25]. Although the implementation requires a numerical treatment, its results can be obtained with any desired accuracy and serve as reference values. The second group of tests concerns an elementary electric dipole in air, oscillating at a frequency of 2.5 GHz. In the FDTD method the smallest representable dipole is made of a single current element placed along an edge of a Yee cell and therefore is not punctiform as the so-called ''hertzian'' dipole. A deviation of the numerical FDTD field within 5 cell off the radiating element is therefore expected with respect to the ideal solution of the continuous case [15,26]. We consider the electric dipole case because it represents a (primary) source for which (5) holds fully. On the other hand, for the sphere in a plane wave field, only the dielectric structure acts as a (secondary) source for which (5) holds: the simultaneous presence of the incident plane wave beam could perturbate, in principle, the effectiveness of formula (5). Tests were made on a coarse grid of $52 \times 52 \times 52$ cubic Yee cells with $\delta = 1$ cm and $\tau = 16.667$ ps. Each one of a subset of $12 \times 12 \times 12$ Yee cells at the core of the previous grid was then refined with several values of the mesh refinement factor R, starting from $R = 5$. The dielectric spherical structure is entirely implemented and centered on the refined part of the grid. The electric dipole, directed along the z-axis, is centered on the refined part of the grid too and one more cell is added, along z, to both the coarse grid and its refined subset. This is made to achieve full symmetry, because the current element, due to the FDTD nodes spatial distribution, has to be half stepped along its direction.

To analyze the grids behavior during the FDTD runs, we introduce two quantities. The first, denoted by S, characterizes what one would qualitatively call the ''mean electric field'' in the discrete computational domain at a given FDTD time iteration. It is defined as

$$S = \frac{1}{\mathcal{N}} \sum_{\text{cells}} \sqrt{E_x^2 + E_y^2 + E_z^2},$$

where the E_i $(i = x, y, z)$ are the FDTD numerical values of the electric field components in a single Yee cell at a given time iteration and $\mathcal{N}$ the number of cells considered in the sum symbol. S can refer to both the coarse (S_{coarse}) or the refined (S_{refined}) grids, with an obvious change of the E_i. For the refined grid one can take any of the R time sub-iterations corresponding to a given FDTD time iteration (see Fig. 2). In the graphs that follow the quantity $S_{\text{total}} = S_{\text{coarse}} + S_{\text{refined}}$ is reported, normalized to its peak value. Due to the transitory character of the excitation, S raises to a maximum (peak) value after the start of a run, then it should decrease and reach a stationary value which represents the residual numerical noise on the grid. However, if instability occurs, S starts to grow uncontrollably until a numerical overflow condition is reached. The second quantity we introduce, denoted by A, monitorizes the accuracy during the FDTD runs

$$A = \frac{1}{\mathcal{N}} \sum_{\text{cells}} \left| \sqrt{|E_x|^2 + |E_y|^2 + |E_z|^2} - \sqrt{|\mathscr{E}_x|^2 + |\mathscr{E}_y|^2 + |\mathscr{E}_z|^2} \right|,$$

where the E_i $(i = x, y, z)$ here represent the FDTD numerical values of the electric field components in the *frequency domain*, normalized to the incident field and the $\mathscr{E}_i$ $(i = x, y, z)$ are the analytical frequency domain values, again normalized to the incident field. These latter values are precalculated (as mentioned above) before the FDTD run starts, stored and then loaded at runtime. Both E_i and $\mathscr{E}_i$ are complex valued quantities and their absolute values have to be computed. Because the exciting signal has a limited time duration, the semidiscrete Fourier transforms of the responses, which are continuously updated, should get, from a given time iteration onward, no more significant contributes at all and finally represent, if no instability occurs, the true response at the frequency of analysis. The E_i in the formula for A are precisely, at any given time iteration, those partially updated responses. Therefore A measures the mean normalized error on the grid. We calculated it for the refined part of the computational domain only.

To justify our assertion about the potential instability of every subgridding algorithm, we report – Figs. 6–8 – the amplitude spectra of a refined electric field component for mesh refinement factors $R = 5, 9, 13$ in the case of the dielectric sphere. These spectra were obtained by storing the FDTD time evolution values when our spatial filtering procedure was turned *off* and for a number of time iterations so that instability overwhelmed any significant signal response. We have chosen the z component of a refined electric field $\vec{e}$ sampled two cell apart from the $\mathscr{S}'$ interface. Then a fast Fourier transform (FFT) is made on the stored data. In each graph the amplitude spectrum is normalized to its maximum value. The details of the spectra are unpredictable and would not have much to tell us, with the possible exception of the peaks' frequency values. In fact, they indicate where instability originates. As can be seen, although graphs concern with the 3-D case, there is a fair match of the peaks' numbers and frequencies with what is expected in the 1-D case (see the table of critical frequencies in Section 3). Similar results hold for $R = 7, 11, 15$. Next we show how the early defined quantities S and A change when, in the case of the dielectric sphere, the filtering procedure described in Section 4 is turned on. Figs. 9–11 refer to S_{total} for mesh refinement factors of 5, 7 and 9, respectively. As can be seen, without the filter the algorithm described in Section 2 would start to become unstable *before* 1000 FDTD time iterations are completed, with an exponential increase of the field values. One should keep in mind that, when a given number of time iterations is reported on the horizontal axes, the corresponding number of refined grid time iterations is indeed greater by a factor of R. By using the simple second-order (parabolic) filter there is a net gain of more than 3 in the overall duration of the FDTD run, what demonstrates the effectiveness of (5). Note in fact that, in our model of the dielectric sphere, 1000 FDTD time iterations suffice for the exciting pulse to travel a distance more than 10-fold the characteristic length of the volume of space in which the target is embedded. Extending stability well beyond the limit of 1000 ensures that, even with more complex objects or large computational domains, the responses we are

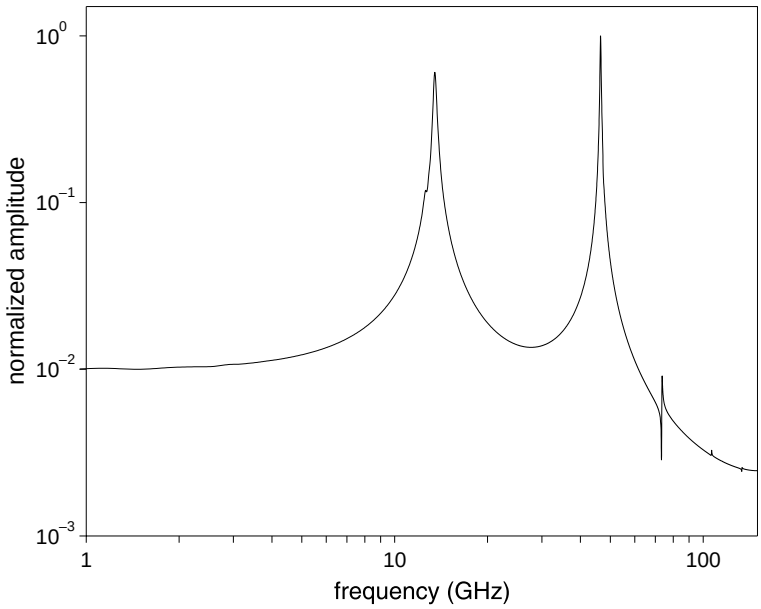

Fig. 6. Two peaks instability after 3100 time iterations when $R = 5$.

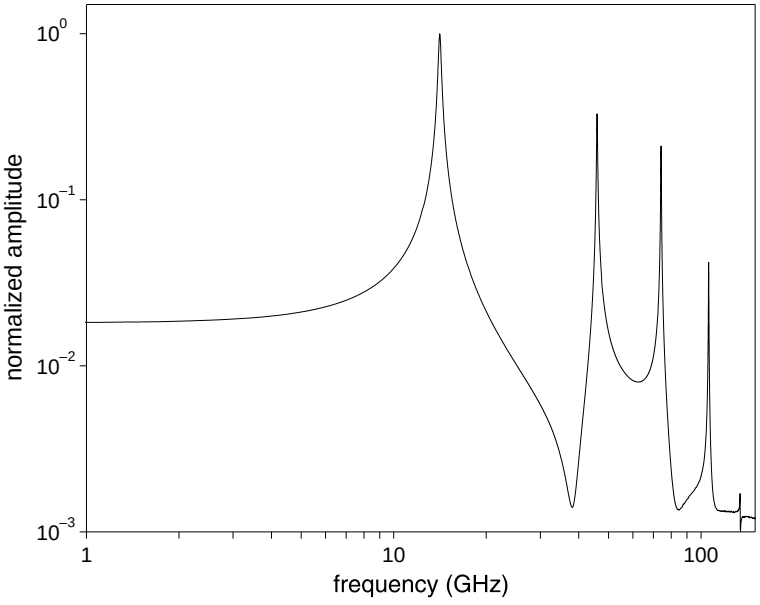

Fig. 7. Four peaks instability after 5100 time iterations when $R = 9$.

now able to analyze permit an accurate determination of the field distribution both inside and outside the target. The fourth-order filter performs almost the same as the second-order one, with a small improvement in its stability. Higher-order filters would track better the response curve of an ideal low-pass filter and with a sharper cut-off, but their implementation suffers a number of problems. Higher-order discrete spatial

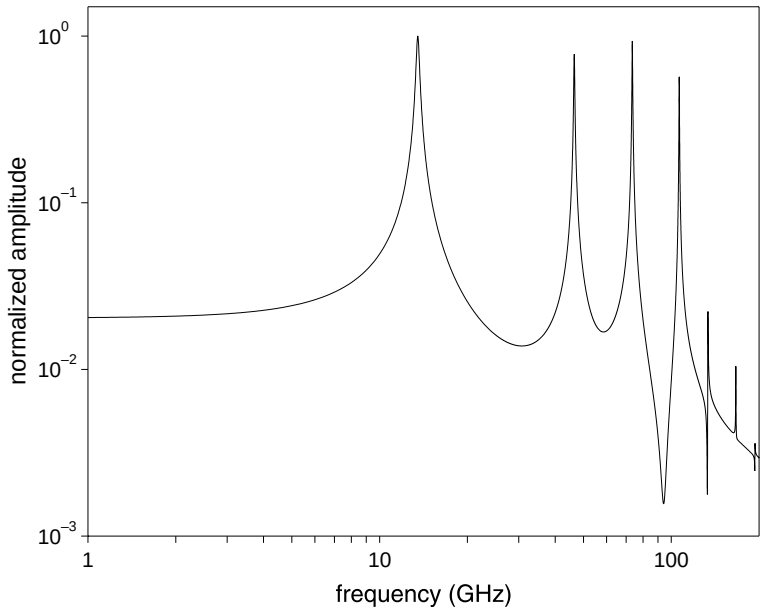

Fig. 8. Six peaks instability after 3100 time iterations when $R = 13$.

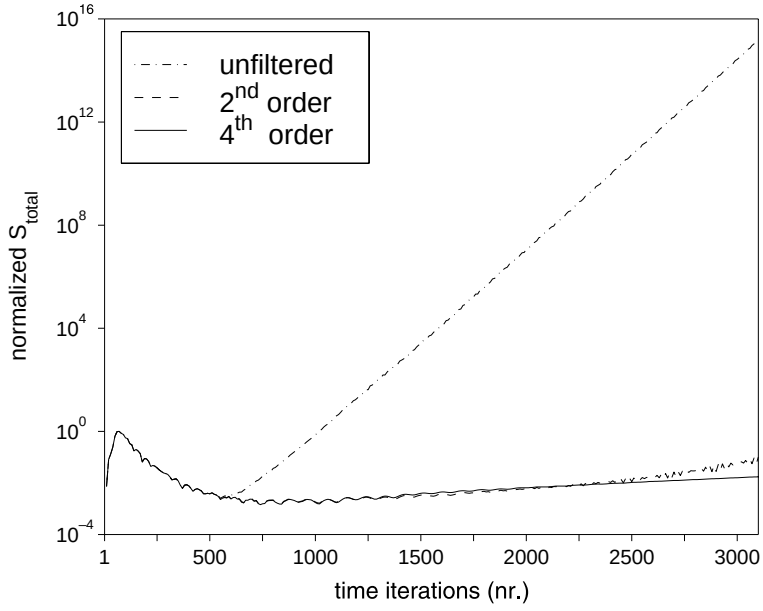

Fig. 9. Preventing instability by spatial filtering when $R = 5$.

derivatives involve sampling points that are far apart the point they are centered on. Moreover, the higher the polynomial degree in the Chebychev expansion, the steepest the growth beyond the interval of approximation, which results, because of the aliasing, in a stronger anomalous amplification of high-

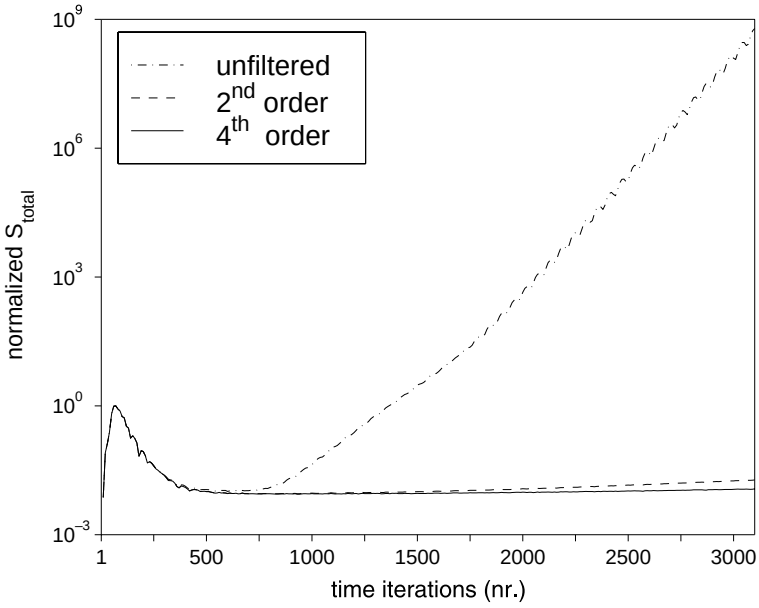

Fig. 10. Preventing instability by spatial filtering when $R = 7$.

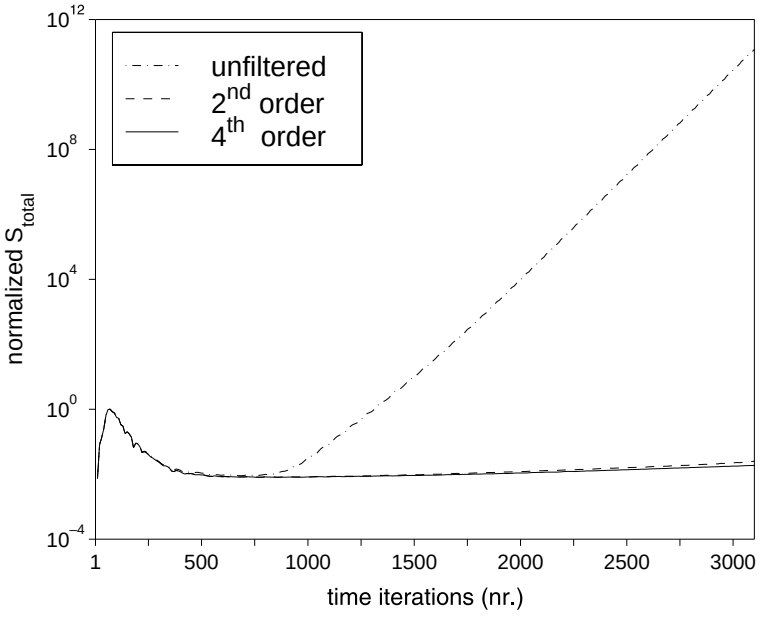

Fig. 11. Preventing instability by spatial filtering when $R = 9$.

frequency low-level noise components. On the other hand it would be an impossible task, by using polynomial approximations, to have a finite passband along with an extremely large stopband while maintaining any reasonable roll-off rate. A specific problem arises when an incident beam is modelled on the

grid. As previously mentioned, (5) applies to fields of primary and secondary sources inside a bounded region in the computational domain. A plane incident wave does not fall into these two categories. Therefore the h^* components used in (5) include incident field contributes that will not be really filtered. As a result of (5) itself, such contributes will superpose noise to the field values due to even order time derivatives of the excitation signal. Its influence is relevant at the higher frequencies only and increases with the order of the filter used, because more time derivatives terms would then be present. That is the reason why one does not expect improvements from an increase in the filter order when an external incident field is taken into account. Fig. 12 compares the percentual accuracy A, for mesh refinement factors of 5, 7 and 9, obtained with the fourth-order spatial filter (accuracies with the second-order filter are a little worse of about 0.1%). The graphs in the figure correspond to those for S_{total} of Figs. 9–11, respectively. As can be seen, once the excitation has been completed, accuracies reach good stationary values that, if the subgridding algorithm is stabilized, are maintained during all of the gained duration of the FDTD runs. Moreover, as one expects, accuracy increases, although slowly, with R. The unfiltered cases are not included in Fig. 12. When the spatial filtering is off, in fact, accuracies first reach minimum values comparable (although a little worse) with the filtered ones then, after the excitation has been completed, errors begin to grow exponentially like S_{total} and accuracy is completely lost. What we would point out here, is the fact that merging FDTD grids of different densities is instability error prone. Such instability is generated at well-defined frequencies. Although the time-domain final result is a global grid numerical overflow, a stable behavior can be imposed by suitably acting on single frequency values. The spectra in Figs. 13 and 14 – which are the counterparts of those in Figs. 6 and 7 – show the ability of spatial filtering to keep unaltered the significant part of the response (below 10 GHz, say), i.e., to recover stability. Being the filters' response curve far from ideal, spurious peaks are seen in the graphs (above 10 GHz) that will ultimately prevail thus permitting only the prolongation, although to a significative and usable extent, of the FDTD runs. Similar results hold for other refinement values. Next, we directly compare – Figs. 15 and 16 – numerical FDTD electric field values with the analytical ones we obtained by applying Stratton's technique. The former are those we calculated *after* the 3100 time iterations – which become 27,900 on the refined grid – of Fig. 11,

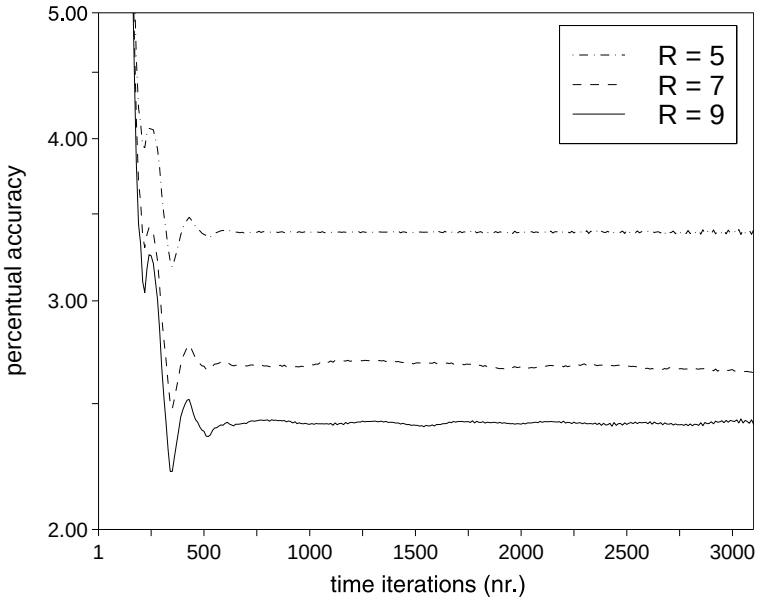

Fig. 12. Percentual accuracy of the stabilized algorithm.

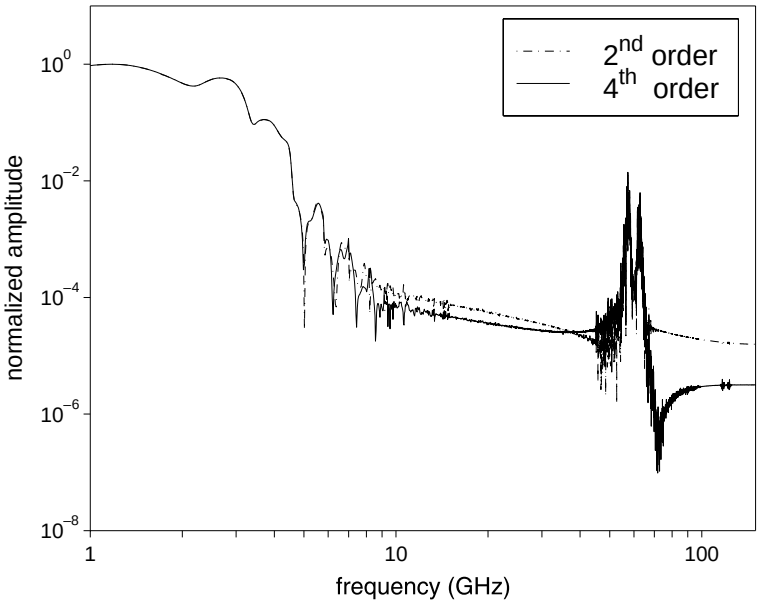

Fig. 13. Amplitudes after 3100 time iterations when $R = 5$.

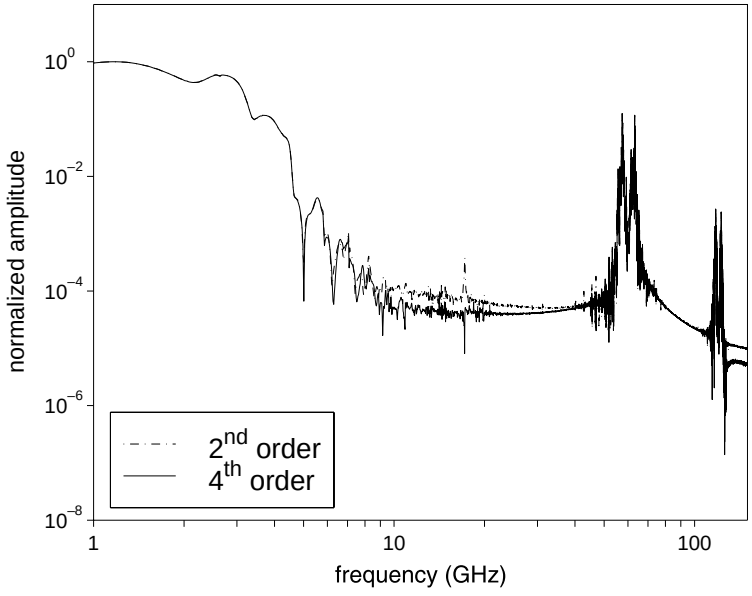

Fig. 14. Amplitudes after 3100 time iterations when $R = 9$.

with $R = 9$ and the fourth-order spatial filter. The comparison is made along an axis parallel to the propagation direction of the incident plane wave beam (from left to right), which we choose as the z-direction, passing through the sphere's center. This latter is located at 26 cm. The plane wave is linearly polarized with the electric field along the x-direction. The data shown are normalized to the incident field

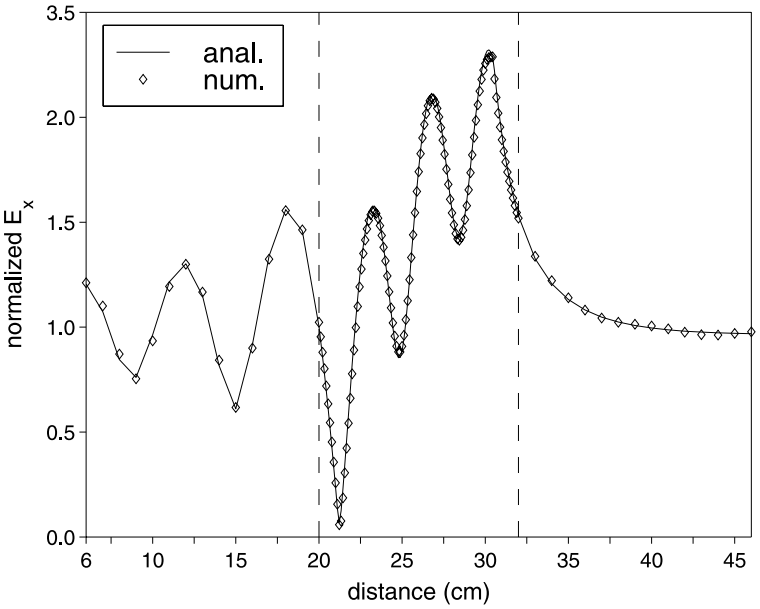

Fig. 15. E_x along z-axis when $R = 9$.

and comprise the resulting electric field components along the polarization (E_x) and propagation (E_z) directions, respectively. Similar graphs, but with no subgridding, have been previously reported in the literature for validation purposes [27]. The vertical dashed lines separate the refined zone of the grid from the coarse one. The analytical solution is indicated by line segments that join the true field component values at the same locations of the numerical sampling points. Note that in Fig. 16, being zero the z component of the electric field on a xz-plane passing through the center of the sphere, we report E_z along an off diameter axis shifted 1 cm apart from that plane. As can be seen there is a very good agreement, better that the global one suggested by Fig. 12. The major error contributions in fact, are due to the staircase approximation of the spherical surface imposed by the FDTD method in rectangular coordinates. Also, in Fig. 16 is detectable a discontinuity of E_z in the transition from inside to outside the dielectric sphere: it follows from the continuity of the normal component of the electric displacement vector $\vec{D}$. Of the entire spatial extension of the computational domain at our disposal, which amounts to 52 cm, only a portion of 46 cm is reported in Figs. 15 and 16. Parts not shown correspond to scattered field zones which come from the method used to include the primary beam. To end the discussion about the dielectric sphere case, we show in Fig. 17 the percentual accuracy A for greater mesh refinement factors – $R = 11, 13$ and 15 – obtained with the fourth-order spatial filter. It should be compared with Fig. 12. As can be seen, there is a further mean accuracy improvement due to a denser sampling points distribution, but also a shortening in the stable operation. The maximum number of FDTD time iterations, in fact, recedes (vertical dashed line) to a value of 2600 (accuracies with the second-order spatial filter are a little worse of about 0.1 and with a larger shortening of about 300). That value, however, now corresponds to 28,600, 33,800 and 39,000 overall time iterations, respectively, on the refined grid. No doubt, our spatial filtering technique demonstrates its effectiveness in preventing and/or mildening error accumulation over a large number of cycles of a FDTD subgridding algorithm. Fig. 18 refers to S_{total} for $R = 15$ and is the analogous of Figs. 9–11. As can be seen, when the spatial filter is turned on there is still a net gain of more than 3 in the overall duration of the FDTD run. The fourth-order spatial filter performs better than the second-order one, because the former has a better coverage of the stopband of an ideal low-pass filter. Raising further the order, however, is not recom-

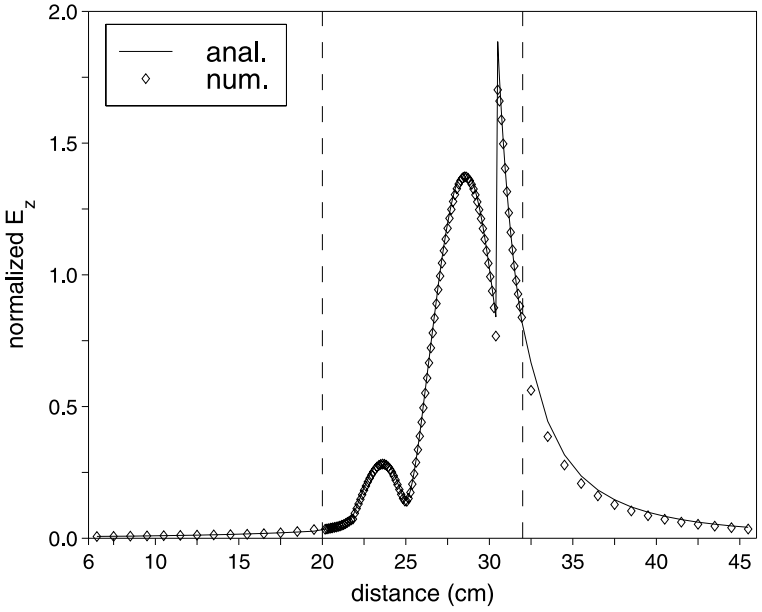

Fig. 16. E_z along z-axis when $R = 9$.

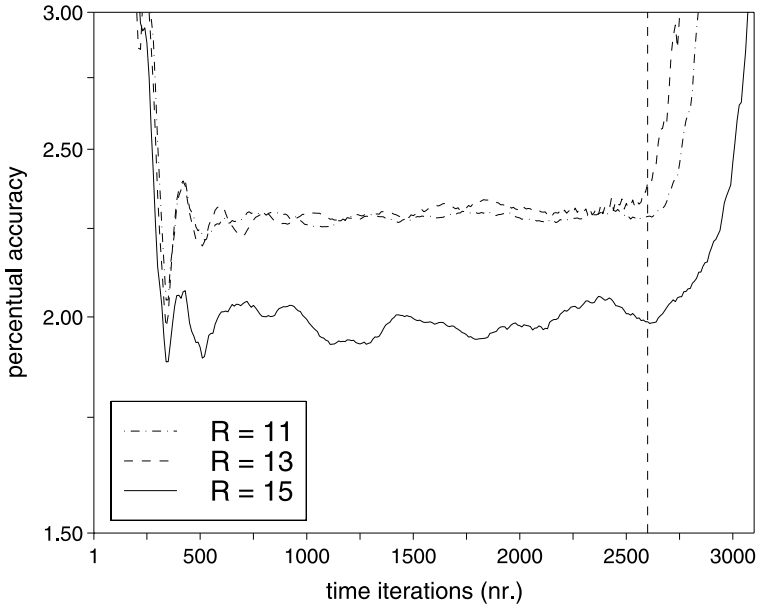

Fig. 17. Percentual accuracy of the stabilized algorithm.

mended in the case of an external primary beam. At the cost of a larger number of floating point operations in fact, there is no performance gain. This is due to the presence of the incident field, as explained above. Our numerical results with the sixth and eighth-order spatial filters, which we do not report here, confirm this circumstance.

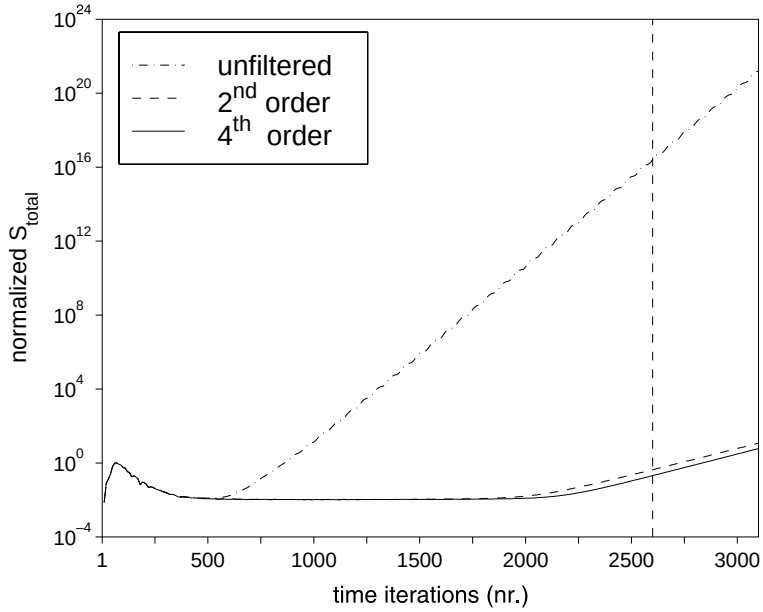

Fig. 18. Preventing instability by spatial filtering when $R = 15$.

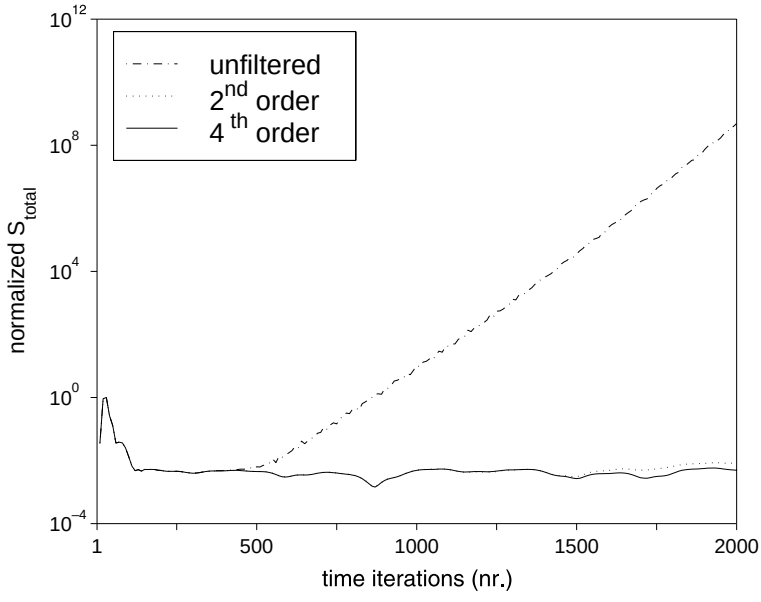

Fig. 19. Preventing instability when $R = 5$. Electric dipole case.

We end this section by discussing briefly the results for the elementary electric dipole. Fig. 19 refers to $R = 5$ with the second- and fourth-order spatial filters. As can be seen, both filters perform almost the same in preventing instability and there is a fourfold gain in the overall number of FDTD time iterations. Fig. 20

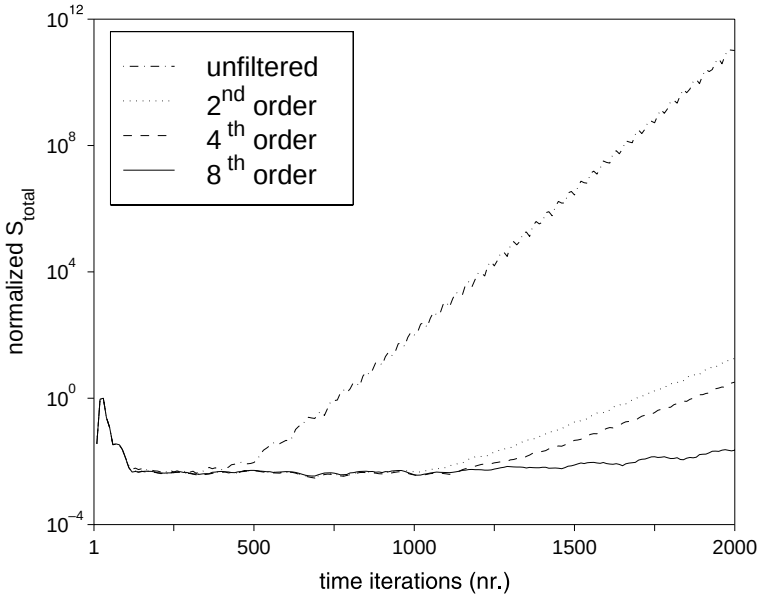

Fig. 20. Preventing instability when $R = 9$. Electric dipole case.

shows that, raising the refinement to $R = 9$, only the eighth-order filer – which cannot be employed with lower values of R – is able to prevent instability until a fourfold gain in the overall number of FDTD time iterations has been reached. The second- and fourth-order ones would have stopped at about 1500 iterations (which are 13,500 for the fine grid). With $R = 15$, the eighth-order filter, for which we do not report graphs, is only able to double the overall duration of the FDTD run and one should resort to stronger filters.

6. Summary

In this paper we have described a subgridding algorithm for the original Yee formulation of the 3-D finite-difference time-domain (FDTD) solution method of Maxwell's equations. Our goal is to keep the overall computational cost as low as possible. The subgridding algorithm here proposed is based on a convenient coupling scheme between the original coarse mesh and the embedded refined one, which minimizes memory allocation and computing times, while allowing the use of the longest admissible time step in each grid of the spatial domain. We demonstrate that mesh refinement renders unstable the FDTD method, due to the presence of high frequency components that are incompatible with the grids' dispersion properties. Therefore, to make our subgridding algorithm robust, we supplement it with a low-pass filtering technique which makes use of a spatial differentiation of the field values involved in the grids' coupling. By using it we achieve, as the numerical experiments demonstrate, the following advantages: (1) to prolong to a large extent the overall number of FDTD time iterations, thus permitting computations with large space domains and/or complex structures, a desired feature in view of the code parallelization; (2) to straightly embed high resolution meshes into a coarse one, thus avoiding the recursive use of multiple nested grids with a progressively increasing resolution (an approach that is currently employed and that rises the computational burden). Our filtering technique does not require extra memory allocation and, in principle, it is usable even with more accurate FDTD formulations other than the Yee one (which we do not consider

in the paper because of their computational cost). Extra times, due to an additional small number of floating point operations, depend on the strengthness of the filtering action, which is adjustable and related to the approximation of an ideal low-pass filter response. The more the terms retained in the approximation, the more effective the beneficial action on the stability, even though highest-order filters do not involve a proportional improvement, especially when fields from sources outside the computational domain are modelled.

References

[1] A. Taflove, Computational Electrodynamics: The Finite-Difference Time-Domain Method, Artech House, Boston, 1995.
[2] K.S. Yee, Numerical solution of initial boundary value problems involving Maxwell's equations in isotropic media, IEEE Trans. Antenna Propagat. 14 (May) (1966) 302–307.
[3] A. Taflove, M.E. Brodwin, Numerical solution of steady-state electromagnetic scattering problems using the time-dependent Maxwell's equations, IEEE Trans. Microwave Theory Technol. 23 (August) (1975) 623–630.
[4] A. Taflove, K.R. Umashankar, Review of FD-TD numerical modeling of electromagnetic wave scattering and radar cross section, Proc. IEEE 77 (May) (1989) 682–699.
[5] S.K. Godunov, V.S. Ryabenkii, Difference Schemes: An Introduction to the Underlying Theory, Elsevier, Amsterdam, 1987, pp. 229–237.
[6] A. Bayliss, E. Turkel, Radiation boundary conditions for wave-like equations, Commun. Pure Appl. Math. 33 (1980) 707–725.
[7] B. Engquist, A. Majda, Absorbing boundary conditions for the numerical simulation of waves, Math. Comput. 31 (July) (1977) 629–651.
[8] G. Mur, Absorbing boundary conditions for the finite-difference approximation of the time-domain electromagnetic-field equations, IEEE Trans. Electromagn. Compat. EMC-23 (November) (1981) 377–382.
[9] L.N. Trefethen, L. Halpern, Well-posedness of one-way wave equations and absorbing boundary conditions, Math. Comput. 47 (October) (1986) 421–435.
[10] R.L. Higdon, Absorbing boundary conditions for difference approximations to the multi-dimensional wave equation, Math. Comput. 47 (October) (1986) 437–459.
[11] R.L. Higdon, Numerical absorbing boundary conditions for the wave equation, Math. Comput. 49 (July) (1987) 65–90.
[12] J.C. Olivier, On the synthesis of exact free space absorbing boundary conditions for the finite-difference time-domain method, IEEE Trans. Antenna Propagat. 40 (April) (1992) 456–460.
[13] J.P. Berenger, A perfectly matched layer for the absorption of electromagnetic waves, J. Comput. Phys. 114 (1994) 185–200.
[14] R. Pontalti, L. Cristoforetti, L. Cescatti, The frequency dependent FD-TD method for multi-frequency results in microwave hyperthermia treatment simulation, Phys. Med. Biol. 38 (1993) 1283–1298.
[15] R. Pontalti, J. Nadobny, P. Wust, A. Vaccari, D. Sullivan, Investigation of static and quasi-static fields inherent to the pulsed FDTD method, IEEE Trans. Microwave Theory Tech. 50 (August) (2002) 2022–2025.
[16] M. Okoniewski, E. Okoniewska, M.A. Stuchly, Three-dimensional subgridding algorithm for FDTD, IEEE Trans. Antenna Propagat. 45 (March) (1997) 422–429.
[17] G.R. Browning, H.O. Kreiss, J. Oliger, Mesh refinement, Math. Comput. 27 (January) (1971) 29–39.
[18] I.S. Kim, W.J.R. Hoefer, A local mesh refinement algorithm for the time domain-finite difference method using Maxwell's curl equations, IEEE Trans. Microwave Theory Technol. 38 (June) (1990) 812–815.
[19] S. Wang, F. Teixeira, R. Lee, J. Lee, Optimization of subgridding schemes for FDTD, IEEE Microwave Wireless Comp. Lett. 12 (June) (2002) 223–225.
[20] L.N. Trefethen, Group velocity in finite difference schemes, SIAM Rev. 24 (April) (1982) 113–136.
[21] R.L. Higdon, Initial-boundary value problems for linear hyperbolic systems, SIAM Rev. 28 (June) (1986) 177–217.
[22] L.N. Trefethen, Group velocity interpretation of the stability theory of Gustafsson, Kreiss, and Sundström, J. Comput. Phys. 49 (1983) 199–217.
[23] L.N. Trefethen, Instability of difference models for hyperbolic initial boundary value problems, Comm. Pure Appl. Math 37 (1984) 329–367.
[24] F.G. Friedlander, On the radiation field of pulse solutions of the wave equation, Proc. Royal Soc. London Ser. A 269 (1962) 53–65.
[25] J.A. Stratton, Electromagnetic Theory, McGraw-Hill, New York, 1941, pp. 563–573.
[26] D.N. Buechler, D.H. Roper, C.H. Durney, D.A. Christensen, Modeling sources in the FDTD formulation and their use in quantifying source and boundary condition errors, IEEE Trans. Microwave Theory Technol. 43 (April) (1995) 810–814.
[27] A. Taflove, Application of the finite-difference time-domain method to sinusoidal steady-state electromagnetic-penetration problems, IEEE Trans. Electromagn. Compat. 22 (August) (1980) 191–202.